DEUTSCHES ELEKTRONEN-SYNCHROTRON

DESY 94–195
H1-11/94-401
November 1994

受入
95-1-251
高工研図書室

Recent Results from the H1 Experiment at HERA

H.-U. Martyn
I. Physikalisches Institut, RWTH Aachen

ISSN 0418-9833

NOTKESTRASSE 85 - 22603 HAMBURG

DESY behält sich alle Rechte für den Fall der Schutzrechtserteilung und für die wirtschaftliche Verwertung der in diesem Bericht enthaltenen Informationen vor.

DESY reserves all rights for commercial use of information included in this report, especially in case of filing application for or grant of patents.

To be sure that your preprints are promptly included in the
HIGH ENERGY PHYSICS INDEX,
send them to (if possible by air mail):

DESY **Bibliothek** **Notkestraße 85** **22603 Hamburg** **Germany**	**DESY-IfH** **Bibliothek** **Platanenallee 6** **15738 Zeuthen** **Germany**

ISSN 0418-9833

DESY 94-195
H1-11/94-401
November 1994

RECENT RESULTS FROM THE H1 EXPERIMENT AT HERA

Hans – Ulrich Martyn*
I. Physikalisches Institut, RWTH Aachen
D-52056 Aachen, Germany†

ABSTRACT

Some recent results from the H1 experiment at the HERA ep collider are presented, based on data taken in 1993 with an integrated luminosity of $\sim 0.5\ pb^{-1}$. The topics include deep inelastic scattering (DIS) of neutral and charged currents, photoproduction and searches for new particles beyond the Standard Model.

The analysis of the proton structure function $\mathcal{F}_2(x, Q^2)$ from neutral current DIS in the novel kinematic region of $3.5 \lesssim Q^2 \lesssim 3000\ GeV^2$ and $10^{-4} \lesssim x \lesssim 10^{-1}$ confirms the previously observed steep rise towards low x values. Several inclusive and topological measurements of the hadronic final state are presented to extract the gluon density in the proton and to get information on the onset of the BFKL evolution.

A sizeable fraction of DIS events are diffractive with a large rapidity gap between the current and proton remnant. Their properties, contribution to the proton structure function and interpretation in terms of a pomeron exchange will be discussed.

Multi-jet rates in DIS events are investigated and used to demonstrate the running of the strong coupling constant $\alpha_s(Q^2)$ and to determine its value at the Z pole.

*Invited talk given at the 22nd Annual SLAC Summer Institute Topical Conference, Stanford, August 17 – 19, 1994

†mailing address: DESY, Notkestr. 85, D-22603 Hamburg; e-mail: f34mar@dsyibm.desy.de

The charged current reaction $e^-p \to \nu_e X$ has been measured and exhibits for the first time the effect of the W propagator.

The scattering of almost real photons on protons reveals the structure of the photon. Results on direct and resolved $\gamma\, p$ processes, hard diffractive $\gamma\, p$ scattering and charm production will be discussed.

Finally, new limits on phenomena beyond the Standard Model will be given. They include direct searches for heavy leptons, leptoquarks, leptogluons, R_p-violatinq squarks and indirect searches via contact interactions.

1 Introduction

The $e\,p$ collider HERA at DESY, in which 27.5 GeV electrons collide with 820 GeV protons, gives access to a so far unexplored new kinematic region of lepton nucleon scattering with a rich physics potential. Due to the large centre of mass energy of $\sqrt{s} \simeq 300$ GeV the kinematic phase space rises the observable momentum transfers Q^2 up to $Q^2_{max} \simeq$ few 10^4 GeV^2 by about two orders of magnitude and lowers the detectable Bjorken x values to $x_{min} \lesssim 10^{-4}$ at small Q^2 by about one order of magnitude with respect to fixed target experiments. Furthermore $\gamma\,p$ interactions can be studied over a wide centre of mass energy range of $W_{\gamma p} \simeq 60 \div 270$ GeV.

HERA was commissioned in 1992 with an initial electron energy of 26.7 GeV. The two experiment H1 and ZEUS published very soon first interesting physics results based on an integrated luminosity of $\mathcal{L} = 0.025$ pb^{-1}. In 1993 an improved HERA performance with more colliding bunches allowed to collect about $\mathcal{L} = 0.5$ pb^{-1} per experiment for useful physics analysis. This year the lepton energy was raised to 27.5 GeV. Since the lifetime of the electron beam turned out to be a severe limitation HERA is operated with *positrons* since July 18, 1994. A peak luminosity of $L_{peak} = 4.3 \cdot 10^{30}$ $cm^{-2}s^{-1}$ is now achieved, about 30% of its design value. With the increased e^+ lifetime (factor of ~ 2.5) and a better understanding of the machine as well as of the H1 detector an integrated luminosity of $\mathcal{L} \simeq 4$ pb^{-1} for physics analysis can be expected for the current data taking period.

The topics to be discussed in this talk is a personal selection of the many H1 results from the data taking period 1993 presented elsewhere* during this summer.

2 The H1 Detector

The H1 detector is a large multi-purpose facility, designed to provide an almost hermetic coverage to detect the final states of $e\,p$ scattering: the hadronic energy flow, charged particles and precise lepton (electron and muon) identification and measurement. While the detector is isotropic in azimuth, it extends more towards the forward region (proton and $+z$ direction) in order to accomodate for the

*Contributions to the *International Conference on High Energy Physics*, Glasgow, July 20 - 27, 1994

moving centre of mass system due to the highly asymmetric proton and electron beam energies (see Fig. 1). Details of the H1 detector can be found elsewhere.[1] Some parameters and actual performance figures are given in Table 1.

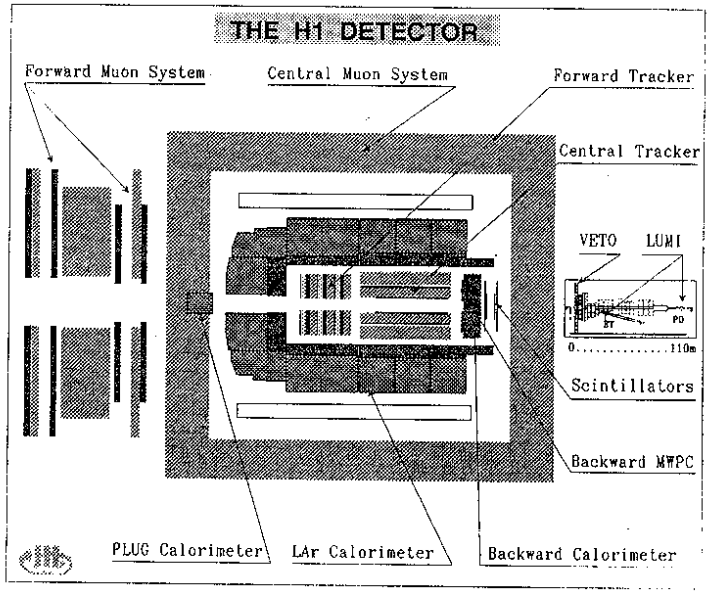

Figure 1: Schematic side view of the H1 detector. The luminosity detector, downstream the electron beam, is not to scale. Protons move to the left ($+z$ direction).

Major emphasis has been given to the calorimetry. The backbone of the detector is a highly transversal and longitudinal segmented liquid argon (LAr) calorimeter. It consists of an electromagnetic and a hadronic section with lead and steel absorbers, respectively. The good hadron energy resolution is achieved by energy weighting techniques during software analysis. The LAr calorimeter provides a very stable response. The absolute energy scales, as determined from test measurements and DIS events, are presently known to 3% (electromagnetic) and 6% (hadronic). A lead-scintillator sandwich calorimeter in the backward region (BEMC) serves mainly to identify and measure the scattered electron in low Q^2 deep inelastic scattering events. A copper-silicon calorimeter (PLUG) covers

Calorimetry		
Liquid Ar Calorimeter	$4° < \theta < 153°$	
granularity (em/hadron)	$10 \div 100\ cm^2$	$50 \div 2000\ cm^2$
depth (em/hadron)	$20 \div 30\ X_0$	$4.7 \div 7\ \lambda_{abs}$
resolution $\sigma(E)/E$ (em/hadron)	$0.12/\sqrt{E_e} \oplus 0.01$	$\sim 0.50/\sqrt{E_h} \oplus 0.02$
BEMC: Pb–scintillator	$151° < \theta < 177°$	
depth – resolution $\sigma(E_e)/E_e$	$22.5\ X_0\ (1\ \lambda_{abs})$	$0.10/\sqrt{E_e} \oplus 0.02$
Tail Catcher: streamer tubes	$4° < \theta < 177°$	
depth – resolution $\sigma(E_h)/E_h$	$4.5\ \lambda_{abs}$	$1.0/\sqrt{E_h}$
Plug Calorimeter: Cu–Si	$0.7° < \theta < 3.3°$	
depth – resolution $\sigma(E_h)/E_h$	$4.25\ \lambda_{abs}\ (45\ X_0)$	$\sim 1.5/\sqrt{E_h}$
e,γ **Tagger**: Tl (Cl/Br)	$\theta > 179.7°$	
depth – resolution $\sigma(E_e)/E_e$	$21\ X_0$	$\sim 0.10/\sqrt{E_e} \oplus 0.01$
Tracking		
Central Tracking	$25° < \theta < 155°$	
spatial resolution	$\sigma_{r\phi} = 170\ \mu m$	$\sigma_z = 2\ mm$
momentum – dE/dx resolution	$\sigma_{1/p} < 0.01\ GeV^{-1}$	$\sigma_{dE/dx} = 10\%$
Forward/Backward Tracking	$7° < \theta < 25°$	$155° < \theta < 175°$
spatial resolutions	$\sigma_{r\phi} = 170\ \mu m$	$\sigma_\theta < 5\ mr$
	$\sigma_{x,y} = 210\ \mu m$	$\sigma_{x,y} = 1\ mm$
Muon Detection		
Instrumented Iron	$4° < \theta < 171°$	
resolutions (barrel)	$\sigma_{r\phi} = 3.5\ mm$	$\sigma_z = 12.5\ mm$
	$\sigma_p/p \approx 0.35$	$\sigma_\theta\ (\sigma_\phi) = 15\ (10)\ mr$
Forward Muon Toroid	$3° < \theta < 17°$	
momentum resolution – range	$\sigma_p/p \sim 0.25$	$5 \div 200\ GeV$

Table 1: Parameters and performance of the H1 detector.

the very forward regions. All calorimeters are placed inside a superconducting coil in order to minimize the inactive material in front of them. The flux return yoke is instrumented with streamer tubes with analogue readout to measure the leakage of hadronic showers (Tail Catcher).

Charged particle tracks are measured in the central and forward tracking systems, placed inside a uniform axial magnetic field of 1.15 T. Each consists of a hybrid of drift and proportional chambers, providing good space information in orthogonal directions as well as some particle identification (dE/dx and transition radiation).

Muon detection and measurement is performed with streamer tubes in the instrumented iron and a dedicated toroidal spectrometer in the forward direction.

A scintillator hodoscope behind the BEMC is used to veto proton-induced background based on its early arrival compared to genuine ep interactions.

The luminosity is determined from the Compton process $ep \to ep\gamma$ at very small scattering angles. The electron tagger (ET) and photon detector (PD) are situated far downstream the electron direction (at $-33\ m$ and $-103\ m$) and serve as well to detect photoproduction events. At present the systematic uncertainty of the luminosity measurement amounts to 5%.

3 Kinematics

The lowest order diagram in the quark-parton model (QPM) of the neutral current (NC) or charged current (CC) process $ep \to e'(\nu)X$ is sketched in Fig. 3, where also the four-vectors involved in the kinematics are defined.

At HERA electrons of 26.7 GeV collide against protons of 820 GeV, giving a total center of mass (cms) energy of $\sqrt{s} = 296\ GeV$. The kinematics is determined by two indepndent variables, conventionally chosen from Q^2, the squared momentum transfer of the exchanged boson, Bjorken x, the momentum fraction of the proton carried by the struck parton, and y, the energy fraction transferred from the incoming lepton to the hadronic system in the proton rest frame. These quantities are related via $Q^2 = x\,y\,s$. The Lorentz invariant kinematic variables are defined as follows:

$$s = 4\,E_e\,E_p \tag{1}$$

$$Q^2 = -(p_e - p'_e)^2 = -q^2 \tag{2}$$

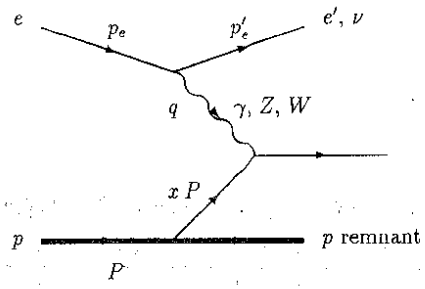

Figure 2: Lowest order diagram (QPM) for $e\,p \to e'\,(\nu)\,X$ and definition of four-vectors

$$y = \frac{P \cdot q}{P \cdot p_e} \tag{3}$$

$$x = \frac{Q^2}{2\,P \cdot q} \tag{4}$$

Since the H1 detector has an almost hermetic $4\,\pi$ coverage, the kinematics can be determined using information from either the scattered lepton or the hadronic final state or a mixture of both (see *e. g.* reference[2]). This redundancy allows to make experimental cross checks and to choose the optimum resolution. The following kinematic reconstruction methods are used in DIS NC analyses.

1. The *electron method*

$$y_e = 1 - \frac{E'_e}{E_e} \sin^2 \frac{\theta_e}{2} \tag{5}$$

$$Q^2_e = 4\,E_e\,E'_e \cos^2 \frac{\theta_e}{2} \tag{6}$$

Q^2_e is always well measured. This method provides good resolutions in a large kinematic region except at low y (high x). The electron method is preferred at high $y > 0.15$.

2. The Σ *method*

$$y_\Sigma = \frac{\sum_h (E_h - p_{z\,h})}{\sum_{e,h} (E - p_z)} \tag{7}$$

$$Q^2_\Sigma = \frac{p^2_{T\,e}}{1 - y_\Sigma} \tag{8}$$

The use of the quantity $\sum_{e,h}(E - p_z) \simeq 2\,E_e$ (h = hadrons) for DIS NC partially removes the large initial state radiative corrections present in the

electron method. The resolutions are good at low y (high x) and still reasonable at low x. The Σ method is preferred at low $y < 0.15$.

3. The *double angle method*

$$Q^2_{da} = \frac{4\,E^2_e\,\sin\gamma\,(1 + \cos\theta_e)}{\sin\gamma + \sin\theta_e - \sin(\gamma + \theta_e)} \tag{9}$$

$$x_{da} = \frac{E_e}{E_p} \cdot \frac{\sin\gamma + \sin\theta_e + \sin(\gamma + \theta_e)}{\sin\gamma + \sin\theta_e - \sin(\gamma + \theta_e)} \tag{10}$$

This method is independent of the absolute energy scales, since only the directions of the electron, θ_e , and the 'struck quark' in the QPM, γ, are used, where

$$\cos\gamma = \frac{(\sum_h p_{x\,h})^2 + (\sum_h p_{y\,h})^2 - (\sum_h (E_h - p_{z\,h}))^2}{(\sum_h p_{x\,h})^2 + (\sum_h p_{y\,h})^2 + (\sum_h (E_h - p_{z\,h}))^2} \tag{11}$$

The resolutions are comparable to the Σ method. The double angle method primarily serves as a cross check.

Experimentally, DIS NC events are rather arbitrarily defined as having a scattered electron detected in the central calorimeters, *i. e.* $\theta_e \lesssim 175°$ or $Q^2 \gtrsim 5\ GeV^2$. The bulk of the data, however, are photoproduction events with a huge cross section, where the electron is scattered under large angles into the backward direction. For tagged electrons $\theta_e > 179.7°$ and $Q^2 \simeq 3 \cdot 10^{-8} \div 10^{-2}\ GeV^2$. The relevant kinematic variables are measured from

$$y = \frac{E_\gamma}{E_e} = 1 - \frac{E'_e}{E_e}\,, \tag{12}$$

$$W_{\gamma p} = \sqrt{y\,s}\,. \tag{13}$$

Besides the interest in the rather inclusive quantities Q^2, x and y many analyses are concerned with topological event properties, such as jet rates and jet properties. Applying any jet algorithm, events are conveniently classified as N+1 jet events. The +1 jet accounts for the proton remnant fragments, of which only a small part is detectable in the calorimeters around the beam pipe. Topologies with 1+1 jets arise from the QPM diagram of Fig. 3, while 2+1 jet configurations may originate from the $\mathcal{O}(\alpha_s)$ processes of boson gluon fusion (BGF, Fig. 3 a) and QCD Compton scattering (Fig. 3 b). The number of observed N jets depends strongly on the jet definition, respectively jet algorithm and resolution parameters used. In

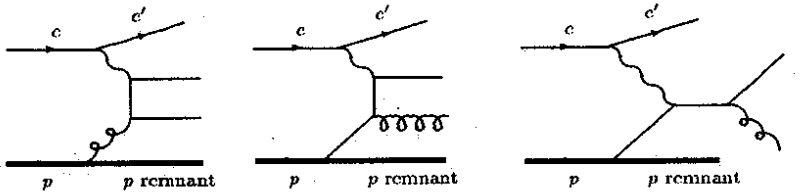

Figure 3: DIS NC processes of $\mathcal{O}(\alpha_s)$ leading to 2+1 jet configurations. **a)** Boson gluon fusion (BGF), **b)** QCD Compton.

2+1 jet events the momentum fraction x_{parton} of the struck parton in the proton can be reconstructed from the invariant mass m_{jj} of the two observed jets

$$x_{parton} = x\left(1+\frac{m_{jj}^2}{Q^2}\right) . \qquad (14)$$

4 The Structure of the Proton

4.1 The Proton Structure Function $\mathcal{F}_2(x,Q^2)$

Neglecting the Z boson exchange, which does not contribute significantly at the present integrated luminosity, the differential cross section for the DIS NC process $ep \to e'X$ can be expressed in terms of the proton structure function $\mathcal{F}_2(x,Q^2)$

$$\frac{\mathrm{d}^2\sigma}{\mathrm{d}x\,\mathrm{d}Q^2} = \frac{2\pi\alpha^2}{xQ^4}\left\{2(1-y)+\frac{y^2}{1+R}\right\}\mathcal{F}_2(x,Q^2) . \qquad (15)$$

The ratio $R=\sigma_L/\sigma_T$ is not yet measured at HERA and is therefore taken from the QCD prescription.

The event selection is based on an integrated luminosity of $\mathcal{L}=271\ nb^{-1}$ and covers the kinematic region $3.5\ GeV^2 \lesssim Q^2 \lesssim 3000\ GeV^2$ and $10^{-4} \lesssim x \lesssim 0.2$. Several independent analyses have been performed using the electron method, the Σ method and the double angle method to reconstruct the kinematics. All analyses agree within each other. The final results are obtained from a combination of the electron and Σ methods, optimizing the kinematic resolutions and minimizing the bin-to-bin migrations. The data are corrected for detector and radiative effects using a Monte Carlo[3] (LEPTO matrix elements + parton showers + QED radiation) with the MRS H[4] input structure function. The overall

systematic uncertainty on the extracted structure function amounts to $\sim$ 10% from the uncertainty in the calorimeter energy scales and 5% from the luminosity measurement (not included in the figures).

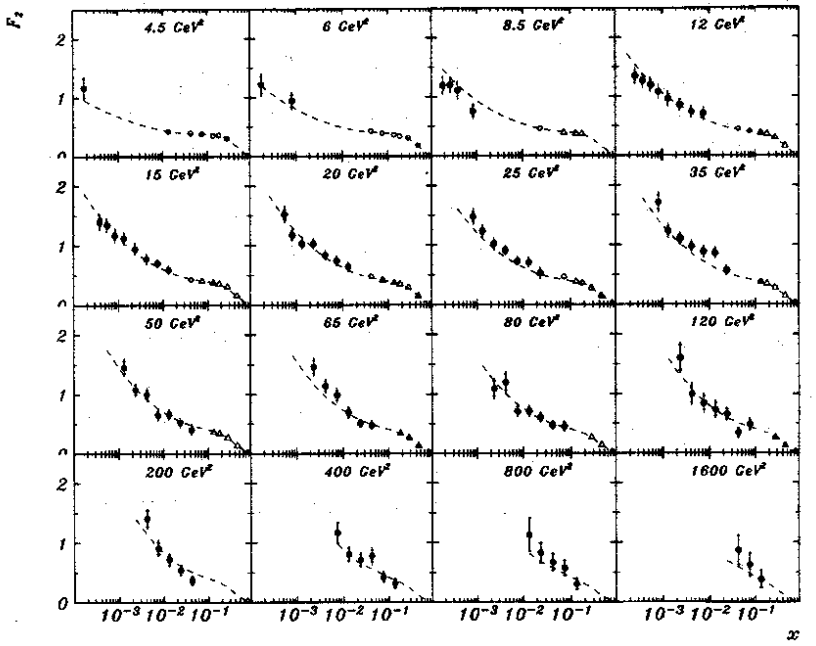

Figure 4: The proton structure function $\mathcal{F}_2(x,Q^2)$ as function of x for several Q^2 intervals. The H1 data (•) are compared with NMC (o) and BCDMS ($\triangle$) measurements. The curves are results of a QCD fit.

The final results on $\mathcal{F}_2(x,Q^2)$ are presented in Fig. 4 as a function of x for various Q^2 bins. The Q^2 dependence of the proton structure function at fixed x intervals is shown in the traditional plot of Fig. 5. The H1 data are in good agreement with the ZEUS results.[5] They are also in agreement with the low energy experiments NMC[6] and BCDMS[7] in the region of overlap. Note the enormous extension of the kinematic phase space with respect to fixed target experiments: about 2 orders of magnitude towards higher Q^2 as well as towards lower x values at small Q^2.

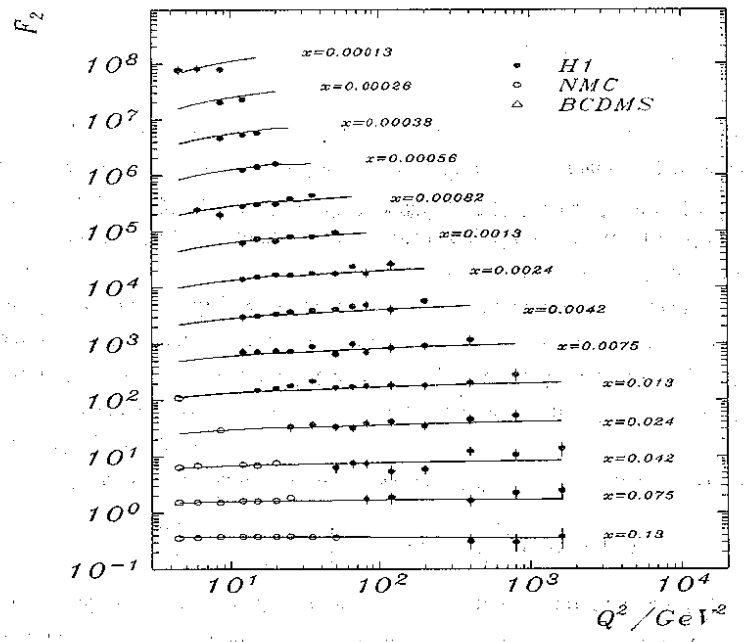

Figure 5: The proton structure function $\mathcal{F}_2(x,Q^2)$ as function of Q^2 for different x intervals, together with data from NMC and BCDMS. The curves are results of a QCD fit. The scale of the $\mathcal{F}_2$ axis has been multiplied by alternating factors of 3 and 10 when going from the highest x bin to lower x bins.

A striking feature is the dramatic rise of $\mathcal{F}_2(x,Q^2)$ at low x seen in Fig. 4, which confirms earlier observations at HERA.[8,9] This rise is attributed to an increased gluon density (and consequently a growing sea quark density) at low x values. Several models have been proposed to describe $\mathcal{F}_2(x,Q^2)$, respectively the parton densities in the proton.

- One approach is to assume a flat gluon density $x\,g(x,Q_0^2) \overset{x\to 0}{\sim}$ const., like MRS D^0 and CTEQ1,[10] or a Regge behaviour.[11] These structure functions generally fall below the data and do not exhibit the observed strong rise.
- Another approach is to assume a rising gluon density $x\,g(x) \sim x^{-\lambda}$, like MRS H, MRS D^- and CTEQ2, but otherwise take the usual DGLAP[12] parton evolutions. Such a singular behaviour is a pure phenomenological

parametrization of the gluon put in by hand. It is motivated by the BFKL[13] evolution predicting $\lambda = 0.5$, in which the summation of large $\log(1/x)$ contributions is taken into account (see section 4.3). These structure functions are able to reproduce the data by a proper choice of $\lambda \sim 0.3$.

- A third approach is to start with input parton distributions at a very low Q_0^2 scale and to evolve them in a double leading logarithm approximation into the HERA regime. An example is the GRV[14] structure function, which descibes the data reasonably well.

A leading order QCD fit[15] has been performed using the DGLAP parton evolution equations with $\Lambda_{QCD} = 240\ MeV$ and 4 flavours. The parton densities have the form $x\,f(x) \sim x^{\beta}(1-x)^{\gamma}(1+\delta\,x+\epsilon\sqrt{x})$. The high x parameters are taken from low energy data as given by the MRS H parton densities, while the low x parameters β and the normalizations are treated as free paramaters. The results of the fit are shown as curves in Figs. 4 and 5 and demonstrate that the data are well described by perturbative QCD.

These new proton structure function measurements in a novel kinematic region will lead to the determination of more reliable parton densities and, in addition, may be used for the calculation of cross sections at very high energy hadron colliders.

4.2 The Gluon Density in the Proton

In order to get insight into the gluon density in the proton several methods have been investigated. One can either use the inclusive measurement of the proton structure function or study the rate of boson gluon fusion processes.

- The leading order QCD fit to $\mathcal{F}_2(x,Q^2)$ of section 4.1 gives for the gluon density and its normalization

$$x\,g(x) \sim x^{-(0.38\pm 0.08)},$$
$$\int x\,g(x)\,dx = 0.57 \quad \text{at} \quad Q_0^2 = 5\ GeV^2.$$

The value of the x-exponent of $\beta_g = -0.38 \pm 0.08$ is close to the one favoured by the BFKL evolution. However, it cannot be concluded that this mechanism is the only explanation for the steep rise of the gluon distribution.

- Using the fact that the $\mathcal{F}_2(x,Q^2)$ scaling violations at low $x \lesssim 10^{-2}$ are dominated by the conversion of gluons into $q\bar{q}$ pairs, one can relate the gluon density directly to the Q^2 dependence of the proton structure function. Prytz[16] derives the following approximation in leading order, from which the gluon density can be extracted

$$\frac{\partial \mathcal{F}_2(x,Q^2)}{\partial \ln Q^2} \simeq \frac{20\,\alpha_s(Q^2)}{27\,\pi}\, x\, g(2x,Q^2)\,. \qquad (16)$$

- A different approach is to analyse boson gluon fusion events with a 2+1 jet topology and jet–jet masses $m_{jj} > 10\,GeV$. The x_{parton} of the struck parton in the proton is reconstructed from eq. 14. Unfolding the x_{parton} distribution and correcting for QCD Compton background ($\sim$ 20%) and migrations ($\sim$ 10%) one gets the gluon distribution in the proton. Due to the event selection, this method gives only access to $x_g \gtrsim 5 \cdot 10^{-3}$.

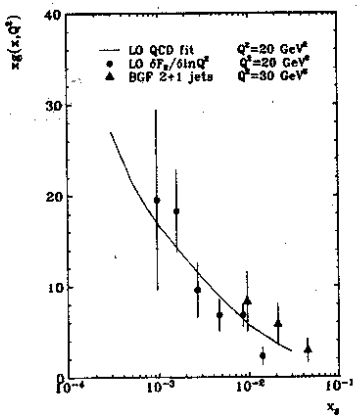

Figure 6: The gluon distribution $x\,g(x)$ in the proton as function of x.

The results of the three analyses are consistent with each other and are displayed in Fig. 6. Despite the still large errors, the data clearly prefer a rising gluon density with decreasing x, as already anticipated by the proton structure function behaviour.

4.3 Evidence for BFKL Evolution?

Many QCD aspects of deep inelastic lepton nucleon scattering are adequately described by the DGLAP[12] evolution equations. However, it is questionable whether this prescription still holds in the low x region accessible at HERA, or has to be supplemented by another parton evolution model. One approach to describe the low x phenomena is the BFKL[13] evolution.

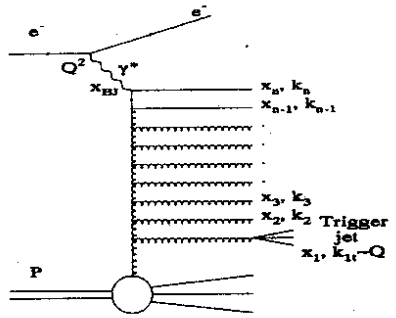

Figure 7: Ladder diagram of deep inelastic $e\,p \to e'\,X$ scattering.

The basic diagram to discuss the features of the DGLAP and BFKL schemes is illustrated in Fig. 7. Before the struck parton hits the virtual photon ($x = x_{Bj}$) to produce a current jet (labeled as n) it may emit a number of gluons.

In the DGLAP scheme the evolution proceeds in $\alpha_s \log Q^2$. The fractional momenta of the gluons decrease along the ladder, $x \le x_n \le \ldots \le x_1$, while the transverse momenta increase and are strongly ordered, $Q^2 \gg k^2_{\perp\,n} \gg \ldots \gg k^2_{\perp\,1}$. As a consequence the transverse energy flow E_T will be depleted between the current and proton and enhanced towards the current direction.

At small $x \lesssim 10^{-2}$ large $\log(1/x)$ terms are encountered, which need to be resummed. This is done in the BFKL scheme, where the evolution proceeds in $\alpha_s \log(1/x)$. The longitudinal momenta of the gluons along the ladder still decrease, $x \ll x_n \ll \ldots \ll x_1$, however, no ordering of the transverse momenta $k_{\perp i}$ is imposed, they undergo a 'random walk'. The diffusion of transverse momenta leads to a reduction of the E_T flow around the current, being shifted towards the proton remnant. Another outcome of the BFKL evolution is the prediction of a

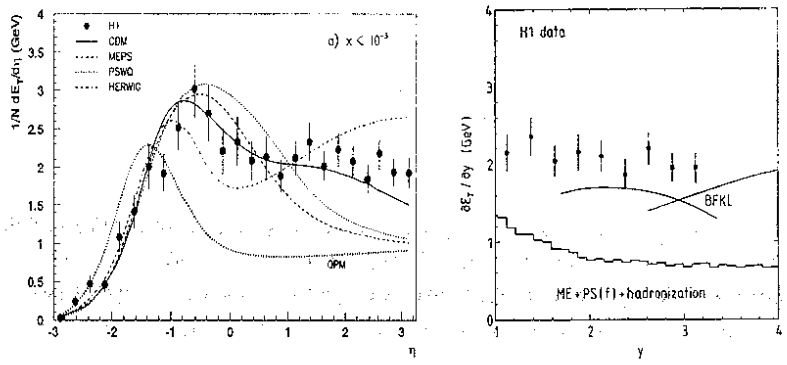

Figure 8: The mean transverse energy flow E_T as a function of pseudorapidity η at $x < 10^{-3}$ and $\langle Q^2 \rangle \simeq 15\ GeV^2$. The proton direction is to the right. a) The H1 data compared to various Monte Carlo models including hadronization. b) The same data compared to an analytic calculation in the BFKL scheme. The histogram indicates the effects of hadronization in the MEPS model.

steeply rising gluon density $x\,g(x) \sim x^{-\lambda}$ with $\lambda = 0.5$.

Thus the most sensitive kinematic phase space to study the onset of BFKL dynamics is the region between the current and proton remnant, $x \ll x_j \ll 1$.

Transverse energy flow 'away' from the current jet[17]

Fig. 8 a shows the mean transverse energy flow E_T as a function of the pseudorapidity $\eta = -\ln\tan(\theta/2)$ in the laboratory system for low $\langle x \rangle \simeq 5.7 \cdot 10^{-4}$ and moderate $\langle Q^2 \rangle \simeq 15\ GeV^2$. The energy flow exhibits an enhancement around the current direction in the central region and levels off at about 2 GeV per unit of rapidity towards the proton remnant at large positive η values. The MEPS model (matrix elements plus parton showers), which uses the DGLAP evolution, produces considerable less energy in the forward region than observed. The colour dipole model[3] (CDM) with quite different dynamics, which supposedly mimics the BFKL behaviour to some extent, is closer to the data.

Recently, analytic calculations at the parton level of the E_T flow using the BFKL scheme have been performed[18], shown in Fig. 8 b. As an illustration the hadronization contribution to the E_T flow is shown for the MEPS model. However, it is not obvious, how the model dependent non-perturbative hadronization

affects the calculations, whether it can just be added. Despite of this, the BFKL expectation of the transverse energy flow 'away' from the current jet is much closer to the data than the expectations from DGLAP based models.

Events with an energetic forward jet

Another 'footprint' for BFKL dynamics may be obtained from the rate of events with an energetic forward jet.[19,20] The sensitivity to the BFKL scheme is enhanced for jets with $k^2_{\perp\,jet} \simeq Q^2$ and $x \ll x_{jet} \ll 1$, where little phase space is left in the DGLAP type evolution (see Fig. 7). Energetic forward jets are defined by a cone algorithm of radius $R = \sqrt{\Delta\eta^2 + \Delta\phi^2} = 1$ and $p_{T,jet} > 5\ GeV$ within $5° < \theta_{jet} < 20°$. DIS events are selected by requiring $x < 2 \cdot 10^{-3}$, $x_{jet} > 0.05$ and $0.5 < p^2_{T,jet}\,/\,Q^2 < 6$ at an average $Q^2 \simeq 20\ GeV^2$.

x range	data	MEPS	BFKL analytic	DGLAP analytic
$2 \cdot 10^{-4} \div 2 \cdot 10^{-3}$	$128 \pm 12 \pm 26$	69	111	45
$2 \cdot 10^{-4} \div 1 \cdot 10^{-3}$	$85 \pm 9 \pm 17$	37	75	25
$1 \cdot 10^{-3} \div 2 \cdot 10^{-3}$	$43 \pm 7 \pm 17$	32	36	20

Table 2: The uncorrected rates of forward jets observed and expected for an integrated luminosity of $\mathcal{L} = 330\ nb^{-1}$. MEPS denotes a full detector Monte Carlo including hadronization. BFKL and DGLAP refer to analytic calculations at parton level.

The number of observed events with an energetic forward jet is given in Table 2 together with some model predictions[20]. The data show a clear increase in the rates by a factor of ~ 2 as x decreases. It is rather the x dependence which should be compared to model predictions, since the absolute values are less reliable. The DGLAP based models – the full MEPS simulation including hadronization and its analytical variant at the parton level – badly fail to describe the observed rise at low x. On the other hand, the analytic BFKL calculation shows a similar x dependence as observed in the data.

Whether these two observations – the enhanced transverse energy flow between the current and proton remnant and the rate of events with an energetic forward